OPEN ACCESS
IOP Publishing | International Atomic Energy Agency Nuclear Fusion

Nucl. Fusion **62** (2022) 076021 (15pp) https://doi.org/10.1088/1741-4326/ac60e8

# Non-parametric inference of impurity transport coefficients in the ASDEX Upgrade tokamak

**T. Nishizawa[1,2,*], R. Dux[1], R.M. McDermott[1], F. Sciortino[1], M. Cavedon[1], C. Schuster[1,3], E. Wolfrum[1], U. von Toussaint[1], A.Jansen Van Vuuren[4,5], D.J. Cruz-Zabala[4,5], P. Cano-Megias[5,6], C. Moon[2] and the ASDEX Upgrade Team[a]**

[1] Max Planck Institute for Plasma Physics, Boltzmannstr. 2, 85748 Garching, Germany
[2] Research Institute for Applied Mechanics, Kyushu University, Kasuga 816-8580, Japan
[3] Physik-Department E28, Technische Universität München, James-Franck-Str 1, 85748 Garching, Germany
[4] Dept. of Atomic, Molecular and Nuclear Physics, University of Seville, Avda. Reina Mercedes, 41012 Seville, Spain
[5] Centro Nacional de Aceleradores (U. Sevilla, CSIC, J. de Andalucia), Seville, Spain
[6] Dept. of Energy Engineering, University of Seville, Spain

E-mail: t.nishizawa@riam.kyushu-u.ac.jp

Received 14 January 2022, revised 6 March 2022
Accepted for publication 24 March 2022
Published 4 May 2022

**Abstract**

We present a non-parametric inference of impurity transport coefficients by using charge exchange recombination spectroscopy measurements of Ne X, Ne VIII, O VIII, and C VI lines. Due to their close atomic numbers, neon, oxygen and carbon impurity ions are assumed to have the same diffusion coefficient $D$ and convection velocity $v$. Unlike conventional techniques that modulate or perturb the impurity contents, we employ a quasi-stationary plasma with static impurity profiles. Since the ratio of $v$ to $D$ only describes the equilibrated profile of the sum of all impurity charge states, steady-state measurements can still decouple $D$ and $v$ if different charge states are simultaneously observed. We have formulated a non-parametric analysis framework based on the Bayesian probability theory and conducted transport coefficient measurements for a Type III ELMy H-mode plasma at ASDEX Upgrade. The charge exchange reactions with the background neutrals, which are known to affect the impurity charge state balance, are taken into account by introducing additional free parameters. While $D$ at the pedestal is close to the neoclassical level ($<1$ m s$^{-2}$), a large diffusion coefficient and a strong outward convection are inferred right inside the pedestal top.

Keywords: tokamak, impurity, Bayesian inference, charge exchange recombination spectroscopy

(Some figures may appear in colour only in the online journal)

* Author to whom any correspondence should be addressed.
[a] See Meyer *et al* 2019 (https://doi.org/10.1088/1741-4326/ab18b8) for the ASDEX Upgrade Team.

## 1. Introduction

Controlling impurity ions is a critical requirement for developing a fusion reactor. Impurity accumulation in the core region hampers the fusion reactions through the fuel dilution and radiates energy away through line radiation and enhanced Bremsstrahlung. However, a proper amount of impurity ions is likely to be required in the edge region in order to mitigate the heat load on the plasma facing components [1, 2]. Furthermore, impurities modify the heat transport and even improve the confinement under some circumstances [3–5]. As such, simply reducing the impurity contents is not sufficient, and achieving controllability of impurity ions by understanding their transport processes is necessary.

Impurity transport is often modeled by using the diffusion coefficient $D$ and the convection velocity $v$ in a simplified cylindrical geometry. Observing time transient impurity emission is a common technique to experimentally determine those transport coefficients. When there is a drastic change in the confinement property, e.g. ELM bursts or the formation of an internal transport barrier, impurity ions redistribute, leading to temporally evolving impurity emission [6–8]. In the case of quasi-stationary plasmas, time-evolving impurity profiles can be created by using techniques such as laser-blow-off [9–11] (LBO), impurity puffing [12], and ion cyclotron resonance frequency modulation [13]. The transient impurity emissions are typically modeled by using an impurity transport solver STRAHL [14], and the $D$ and $v$ profiles that reproduce the observations are inferred. When the measurements provide the time evolution of the total impurity density of one species and its local flux, $D$ and $v$ can be more directly determined from the transport equation [6, 12]. Recently, a systematic study on the model selection in the $D$ and $v$ measurements using LBO and x-ray spectroscopy has been conducted [9]. The study reports that the inference problem of $D$ and $v$ is ill-posed in the assumed diagnostic setup, and the inference results strongly depend on the choice of the model functions used for representing the profiles. When the model functions are too simple, the inferred $D$ and $v$ profiles can be quite different from the true ones, and the uncertainties become unrealistically small even though the forward model is in a seemingly reasonable agreement with the data. These results indicate that addressing the model selection problem and properly estimating uncertainties are crucial in the impurity transport coefficient measurements. Reference [9] concludes that this can be achieved by a Bayesian approach.

Several references [11, 15–17] have already reported impurity transport studies by using the Bayesian formalism. In these approaches, the probability distribution for the $D$ and $v$ profiles, which is called the prior, is first defined without considering the data. Then, by multiplying this prior distribution by the likelihood, which depends on the data, we obtain the results of the $D$ and $v$ profile measurements, the posterior. Since the Bayesian method calculates the probability distribution for obtaining given pairs of $D$ and $v$ profiles, the robust uncertainty estimation is possible not only for $D$ and $v$, but also for their ratio by taking into account their correlation. In addition, the optimum model function can be selected among many candidates by evaluating the Bayes factors [9, 11]. An additional advantage of the Bayesian approach is the coherent combination of multiple diagnostics, which is referred to as integrated data analysis (IDA) [18]. The sum of information from various diagnostics provides a more localized likelihood and improves the ill-posed conditions. References [15, 16] combined charge exchange spectroscopy (CXRS), vacuum ultraviolet spectroscopy, and soft x-ray measurements and inferred the $D$ and $v$ profiles that are consistent with all the diagnostics.

The model selection is also an important problem for more fundamental plasma parameters such as the electron density $n_\mathrm{e}$ and the electron temperature $T_\mathrm{e}$. For these parameters, non-parametric inference techniques based on the Gaussian processes are often used [19–21]. In a non-parametric approach, each spatial grid point has its own degree of freedom, and the prior specifies the correlation between spatial points by using a probability distribution such as the Gaussian process. By tuning this probability distribution the properties that plasma parameters are expected to have, e.g., the degree of smoothness and variation, can be imposed. For this reason, the posterior given by the non-parametric approach is not restricted to piecewise connected cubic functions, which is the case for cubic splines and contains all possible solutions that are consistent with the data and the prescribed properties of the profile. Due to its complete search of the solution space, even second derivatives of the original profile can be evaluated by using a non-parametric inference technique [22]. The difference between parametric and non-parametric inferences is further discussed in appendix A. High degrees of freedom, however, lead to a large computation cost, and the application of the non-parametric profile inference was originally limited to the cases where the posterior distribution can be calculated analytically. With the advent of efficient algorithms [23–25], non-parametric approaches have been applied to complex models in recent years [26, 27].

This paper reports the non-parametric inference of the impurity transport coefficients for the first time. In order to make the complex high dimensional problem tractable, we employ an unconventional diagnostic setup. Instead of modulating the impurity contents, we utilize a plasma in a quasi-stationary state and measure multiple impurity emission lines from different charge states by using CXRS. When only a fully-ionized state is present in a steady state plasma, the continuity equation is given by: $\mathrm{d}n_Z/\mathrm{d}r = vn_Z/D$, where $n_Z$ is the impurity density, and $r$ is the radius. Thus, we can only probe the ratio of $v$ to $D$. However, when lower charge states have significant populations, source and sink terms cannot be neglected, and multiple continuity equations of different charge states, which couple to each other, need to be evaluated. In this case, $D$ and $v$ can be separated by measuring different charge states. Indeed, simultaneous modeling of $D$ and $v$ in quasi-steady state plasmas by using multiple charge state measurements has already been reported [28, 29]. One of

the advantages in this technique is that the steady-state impurity profiles can be determined analytically for given background plasma parameters and impurity transport coefficients. A steady state also allows for time averaging over a long interval, and precise measurements become possible. In addition, we take into account the charge exchange reactions due to the background thermal neutrals, which has been shown to have a large influence in the charge state balance [17, 30].

This paper is organized as follows. Section 2 describes the experimental scenario and the diagnostic setup. The analysis procedure formulated within the Bayesian framework is presented in section 3. The results of the impurity transport coefficient inference are given in section 4. Finally, section 5 presents the conclusions.

In this paper, we use a lower subscript and a vector to represent a radial position and a profile, respectively, e.g., $n_{\mathrm{e},n}$ is the value of $n_\mathrm{e}$ at the radial position of $n$, and $\vec{n}_\mathrm{e}$ is the profile of $n_\mathrm{e}$. As for the impurity ions, which have multiple charge states, a vector without a charge state index represents the profiles of all charge states except the neutral state, e.g., $\vec{n}_\mathrm{Ne}$ is a symbol for the neon ion profiles from $\vec{n}_{\mathrm{Ne}^{1+}}$ to $\vec{n}_{\mathrm{Ne}^{10+}}$.

## 2. Impurity density measurements using charge exchange spectroscopy

Charge exchange recombination spectroscopy (CXRS) [31] provides localized impurity density measurements. Impurity ions in the plasma undergo charge exchange reactions with energetic neutral hydrogen or deuterium atoms introduced by neutral beam injection (NBI). This electron transfer brings impurity ions into a lower charge state and leaves them in excited states. CXRS measures line emission associated with the relaxation of those impurity ions. Since this process occurs along the trajectory of the neutral beam, the emission intensity, impurity velocity, and temperature near the intersection between a line of sight (LOS) and the neutral beam can be obtained through line-shape analysis. The spectral radiance due to the beam-induced charge exchange reaction at wavelength $\lambda$ is given by:

$$L_\lambda = \int_{\mathrm{los}} n_z \nu_z^\lambda \,\mathrm{d}s, \tag{1}$$

where $n_z$ is the impurity density, and the integral los is along the LOS. The rate coefficient $\nu_z^\lambda$ is a rather complicated function of local plasma parameters, the energy components of the neutral beam and their spatial profiles. We use the charge exchange impurity concentration analysis code COLRAD to calculate $\nu_z^\lambda$. COLRAD takes into account important effects: the beam divergence and attenuation, the halo contribution, and the populations of the beam neutrals in the excited states. The detailed description can be found in reference [32].

Using CXRS, we measured three emission lines Ne X 524.49 nm, Ne VIII 606.9 nm, and C VI 529.07 nm. In the vicinity of Ne VIII 606.9 nm, there is another emission line O VIII 606.9 nm. These lines cannot be discriminated, and we can only calculate the sum of $n_{\mathrm{Ne}^{8+}}$ and $n_{\mathrm{O}^{8+}}$. Not that Ne VIII 606.9 nm and O VIII 606.9 nm have almost identical $\nu_z^\lambda$. The LOSs for CXRS and the magnetic geometry of the plasma are shown in figure 1. A steady neon puff of $8.8 \times 10^{20}$ atoms $\mathrm{s}^{-1}$ was applied to a Type-III ELMy H-mode discharge in the ASDEX Upgrade tokamak (AUG). The profiles of the electron density $n_\mathrm{e}$, the electron temperature $T_\mathrm{e}$, and the ion temperature $T_\mathrm{i}$ are shown in figure 3 in section 4 where the results of the transport coefficient measurements are discussed. Other main plasma parameters are $I_\mathrm{p} = 0.6$ MA, $\kappa = 1.65$, and $\delta = 0.38$ where $I_\mathrm{p}$, $\kappa$, and $\delta$ are the plasma current, elongation, and triangularity, respectively. The external heating of 7.5 MW was provided by NBI, and 2.5 MW by electron cyclotron heating. NBIs were modulated to allow for the subtraction of passive emission. When the NBI, on which the LOSs are focused, was off, another NBI was turned on such that the NBI heating power stayed constant. The plasma was quasi-stationary from 6.2 to 8.7 s. We calculated the time-averaged net intensities of active charge exchange emission (including Type-III ELMs) during this period by subtracting the passive intensities.

**Table 1.** Combinations of spectrometer, optical head and emission line in the charge exchange recombination spectroscopy measurements.

| Spectrometer | Optical head | Emission line(s) |
|---|---|---|
| CER | A | 524 nm (Ne X), 529 nm (C VI) |
| CMR | B, C | 524 nm (Ne X), 529 nm (C VI) |
| CAR | A | 607 nm (Ne VIII + O VIII) |
| CPR | B, C | 607 nm (Ne VIII + O VIII) |

Figure 1 shows the viewing geometry of the CXRS measurements. The LOSs originate from three different optical heads A, B, and C, and each head houses a lens and a bundle of optical fibers. Different colors are used to trace the LOSs depending on their optical heads. At the marker locations, the LOSs intersect with the 60 keV neutral beam. The core regions are measured by head A with the spatial resolution of a few cm, while the pedestal region is probed by head B and head C with higher spatial resolution (sub-cm). In this measurement, we used four spectrometers: CER, CMR, CAR, and CPR. The setup of the spectrometers, optical heads and the measured emission lines are summarized in table 1. We take into account these combinations when estimating systematic uncertainties in section 3.5. The data points of CXR measurements are shown in figure 6 in section 4 together with the forward-modeled data.

## 3. Analysis

### 3.1. Modeling impurity transport

In the confined region, the continuity equation of impurity ions with an atomic number $Z$ is given by [28]:

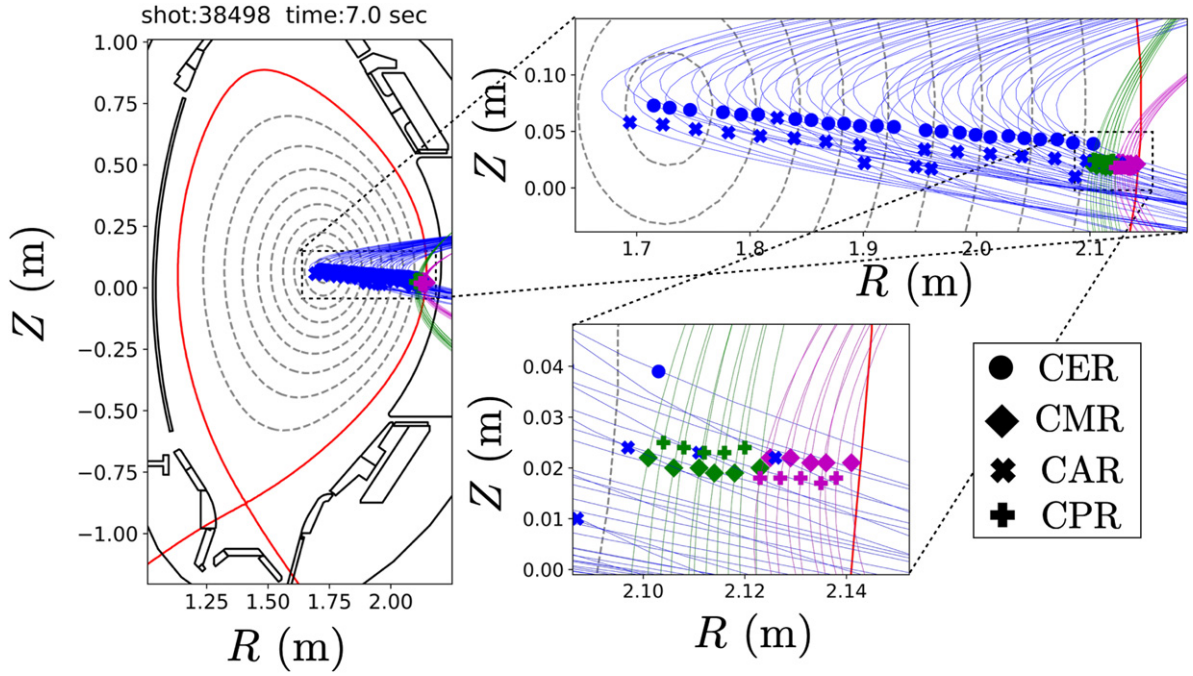


**Figure 1.** Flux surfaces of the ASDEX Upgrade plasma in the Type-III ELM regime and lines of sight (LOS) for the charge exchange recombination spectroscopy measurements. The LOSs are projected onto the poloidal surface. The red solid line is the last closed flux surface. The blue lines are the lines of sight from optical head A while the green and the magenta lines are from optical head B and C, respectively. Markers are placed at the intersections between the neutral beam and the LOS. The shapes of the markers represent the spectrometers, to which the lines of sight are connected. More details about the CXR system at AUG are discussed in reference [33].

$$\frac{\partial n_z}{\partial t} = -\frac{1}{r}\frac{\partial}{\partial r}(r\Gamma_z) + \left(R_{z+1}n_\mathrm{e} + R^{\mathrm{cx}}_{z+1}n_0 + \sum_i R^{\mathrm{cx,\,b}}_{z+1,i}n^{\mathrm{b}}_{0,i}\right)n_{z+1} - \left\{(I_z + R_z)n_\mathrm{e} + R^{\mathrm{cx}}_z n_0 + \sum_i R^{\mathrm{cx,\,b}}_{z,i}n^{\mathrm{b}}_{0,i}\right\}n_z + I_{z-1}n_\mathrm{e}n_{z-1}, \tag{2}$$

where $t$ is time, $r$ is the radius, and $n_0$ is the neutral density except the beam neutrals. $z = 2, 3, 4, \ldots, Z-1$ represents a charge state. The continuity equations for $z = 1$ and $z = Z$ can be obtained by removing interactions with lower and higher charge states from equation (2), respectively. In this one dimensional model, $r \equiv \sqrt{V/(2\pi^2 R_{\mathrm{axis}})}$, where $V$ is the volume enclosed by a flux surface, and $R_{\mathrm{axis}}$ is the major radius at the magnetic axis. $R_z$ and $I_z$ are the effective recombination and ionization coefficients, respectively, which depend on $n_\mathrm{e}$ and $T_\mathrm{e}$. The charge-exchange recombination rate with thermal neutrals is given by $R^{\mathrm{cx}}_z$. An explicit expression of this rate coefficient is [34]

$$R^{\mathrm{cx}}_z = \sum_q f_q(n_\mathrm{e}, T_\mathrm{e})Q_q(T_{\mathrm{red}}), \tag{3}$$

where $T_{\mathrm{red}} \equiv (T_\mathrm{i}m_\mathrm{D} + T_0 m_Z)/(m_\mathrm{D} + m_Z)$ is the reduced temperature. $T_\mathrm{i}$ and $T_0$ are the impurity ion temperature and the neural particle temperature, respectively. $m_\mathrm{D}$ and $m_Z$ are the masses of the deuterium atom and the impurity ion. $f_q$ is a fraction of $n_0$ in a quantum state $q$. For each $q$, $Q_q$ defines the charge exchange recombination rate coefficient. $n^{\mathrm{b}}_{0,i}$ and $R^{\mathrm{cx,\,b}}_{z,i}$ are the beam neutrals and their recombination rate coefficient for the beam energy component $i$ and the impurity charge state $z$, respectively. The energy components of NBIs and their profiles have already been characterized at AUG [32]. Since we can determine $R^{\mathrm{cx,\,b}}_{z,i}$ by using the charge exchange cross section provided by reference [35], the recombination due to the beam neutrals is treated as a known quantity in the present work. We use the diffusion coefficient $D$ and the convection velocity $v$ to model the particle flux $\Gamma_z$ as follows:

$$\Gamma_z = -D\frac{\partial n_z}{\partial r} + vn_z. \tag{4}$$

In this transport model, the same transport coefficients $D$ and $v$ are used for all charge states of the three different impurity species: carbon, oxygen, and neon.

In the SOL, we add a parallel loss term $-n_z/\tau_\parallel$ to the rhs of equation (2), where

$$\tau_\parallel^{-1} \equiv \frac{2M_v}{L_\parallel}\sqrt{\frac{3T_\mathrm{i} + T_\mathrm{e}}{m_\mathrm{D}}}. \tag{5}$$

Here, $M_v$ is the Mach number, and $L_\parallel$ is the connection length. We set $M_v = 0.1$ and $L_\parallel = 25$ m, which are often used for AUG plasmas [7, 8]. While this modeling for the parallel loss effect is somewhat ad hoc, the inference results in the confined region are relatively insensitive to the details in the SOL, which will be shown in section 4.

### 3.2. Modeling the neutral profile

We model the transport process of neutral particles using a Monte Carlo code in a cylindrical geometry [30]. Neutral deuterium atoms are released from the wall with the energy $E_{0,\mathrm{wall}}$. When ionization happens, tracking of the deuterium atom ends at that location. When it experiences a charge exchange recombination event, the velocity of the tracking particle is replaced by that of the ion involved in the reaction. The frequencies of ionization and charge-exchange events at each radial location are determined by the background plasma profile. In this model, the profiles of $n_0$ and the neutral temperature $T_0$ are determined by $E_{0,\mathrm{wall}}$ and the neutral density at the wall $n_{0,\mathrm{wall}}$. We use these two quantities as free parameters to describe $\vec{n}_0$ and $\vec{T}_0$.

### 3.3. Prior

We introduce a prior that defines the probability distribution of the parameters of interest before measurements are made. $\vec{T}_0$ and the relative profile shape of $n_0$ for a given energy at the wall $E_{0,\mathrm{wall}}$ are uniquely determined by using the Monte Carlo code discussed in section 3.2. We calculate $\vec{T}_0$ and the profile shapes of $n_0$ for $E_{0,\mathrm{wall}} = 10$, 20, 40, 80, and 120 eV. By interpolating those profiles, $\vec{n}_0$ and $\vec{T}_0$ for arbitrary $E_{0,\mathrm{wall}}$ between 10 and 120 eV can be obtained without running the Monte Carlo code again. We use the neutral density at the wall $n_{0,\mathrm{wall}}$ to determine the absolute density, and define the prior distribution of $\vec{n}_0$ and $\vec{T}_0$ as

$$\begin{aligned} &p(\vec{n}_0, \vec{T}_0 | E_{0,\mathrm{wall}}, n_{0,\mathrm{wall}}) p(E_{0,\mathrm{wall}}) p(n_{0,\mathrm{wall}}), \\ &p(E_{0,\mathrm{wall}}) \propto 1/E_{0,\mathrm{wall}} \quad 10\ \mathrm{eV} \leqslant E_{0,\mathrm{wall}} \leqslant 120\ \mathrm{eV}, \\ &p(n_{0,\mathrm{wall}}) \propto 1/n_{0,\mathrm{wall}} \quad 10^4\ \mathrm{m}^{-3} \leqslant n_{0,\mathrm{wall}} \leqslant 10^{18}\ \mathrm{m}^{-3}. \end{aligned} \tag{6}$$

Here, we choose logarithmic priors for $p(E_{0,\mathrm{wall}})$ and $p(n_{0,\mathrm{wall}})$ to avoid a bias toward high amplitudes [36, 37].

Since equation (2) is linear with respect to $n_z$, the profile of each charge state for given $\vec{D}$ and $\vec{v}$ can be solved analytically. The analytical solution and its derivation are given in appendix B. We use the Gaussian process and introduce the probability distribution of $\vec{D}$ as follows:

$$\begin{aligned} p(\vec{D}|\hat{\Sigma}) &\propto \exp\left(-\frac{1}{2}\vec{\theta}^{\intercal}\hat{\Sigma}^{-1}\vec{\theta}\right) \\ \vec{\theta}^{\intercal} &= [\log_{10} D_1, \log_{10} D_2, \ldots, \log_{10} D_N], \end{aligned} \tag{7}$$

where

$$\hat{\Sigma}_{n,n'} = \sigma_D^2 \exp\left(-\frac{(r_n - r_{n'})^2}{2l_{\mathrm{co}}^2}\right). \tag{8}$$

$$\sigma_D = 1. \tag{9}$$

Note that the Gaussian process provides the profile of $\log_{10} D$ instead of $D$. This parameterization avoids a bias toward a larger scale and removes negative $D$, which is unphysical. Other impurity transport studies by using the Bayesian framework also infer the power of $D$ [11, 15, 16]. The spatial correlation length $l_{\mathrm{co}}$ shown in figure 2 is set to be proportional to the spacing between spatial grids. $l_{\mathrm{co}}$ is reduced near the pedestal region, where large variations in $D$ and $v$ over small spatial scales are expected.

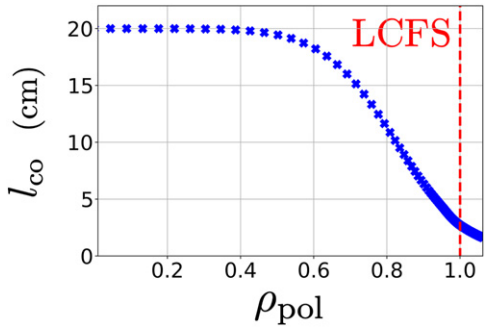


**Figure 2.** Correlation length $l_{\mathrm{co}}$ used for equations (8) and (11) vs the radial grid points. The location of the last closed flux surface is shown by the red dashed line.

Instead of defining the prior distribution of $\vec{v}$ directly, we introduce the probability distribution of $\int_0^r v\,\mathrm{d}r'/D$. This parametrization leads to a significantly better performance of MCMC compared with the direct parametrization of $\vec{v}$. In equation (B.4), $v$ is contained only in the form of $\int_r^{r_{\mathrm{edge}}} v\,\mathrm{d}r'/D$. Thus, the original parameter space becomes simpler when we use $\int_0^r v\,\mathrm{d}r'/D$. The probability distribution of $\vec{v}$ can still be calculated when all constituents of the prior distributions are multiplied. First, we use the Gaussian process again to define:

$$p(\vec{\psi}|\hat{\Omega}) \propto \exp\left(-\frac{1}{2}\vec{\psi}^{\intercal}\hat{\Omega}^{-1}\vec{\psi}\right), \tag{10}$$

where

$$\hat{\Omega}_{n,n'} = F^2 \exp\left(-\frac{(r_n - r_{n'})^2}{2l_{\mathrm{co}}^2}\right). \tag{11}$$

Using $\psi$, we define the discrete form of $\int_0^r v\,\mathrm{d}r/D$ as follows:

$$\sum_{i=1}^{n} \frac{v_i}{D_i}\Delta r_i = (\psi_n - \psi_1) - (F + \psi_n - \psi_1)\cdot\frac{r_n}{r_N}. \tag{12}$$

By this definition, $\int_0^r v\,\mathrm{d}r'/D$ varies from 0 to $-F$. The profile shape of $\sum_{z=1}^{Z} n_z$ is proportional to $\exp\left(\int_0^r v\,\mathrm{d}r/D\right)$ in the confined region. Thus, the sum of all charge states of one impurity species varies by a factor of $\mathrm{e}^{-F}$ from the core to the edge if there is no parallel loss term in the SOL. We use $F = \ln 2$ in this inference problem. We found that equation (12) leads to a smaller autocorrelation of MCMC samples, and reduces the computation expense compared with the other parameterizations that had been tested. Using equations (10)–(12), we define the conditional probability density $p(\vec{v}|\hat{\Omega}, \vec{D})$.

In addition to the rate coefficients, $\vec{D}$, and $\vec{v}$, the boundary conditions for each charge state need to be specified in order to calculate impurity density profiles using equation (B.15). We use the ratios between charge states when there is no transport at the edge, and introduce the line-averaged highest charge state density $\bar{n}_Z \equiv \int_0^{r_{\mathrm{edge}}} n_Z\,\mathrm{d}r/r_{\mathrm{edge}}$, for which we have a good estimate from the CXRS measurements, as a parameter for specifying the absolute impurity densities. As discussed in appendix B, the edge boundary conditions have a small impact on the profile shapes in the confined region when

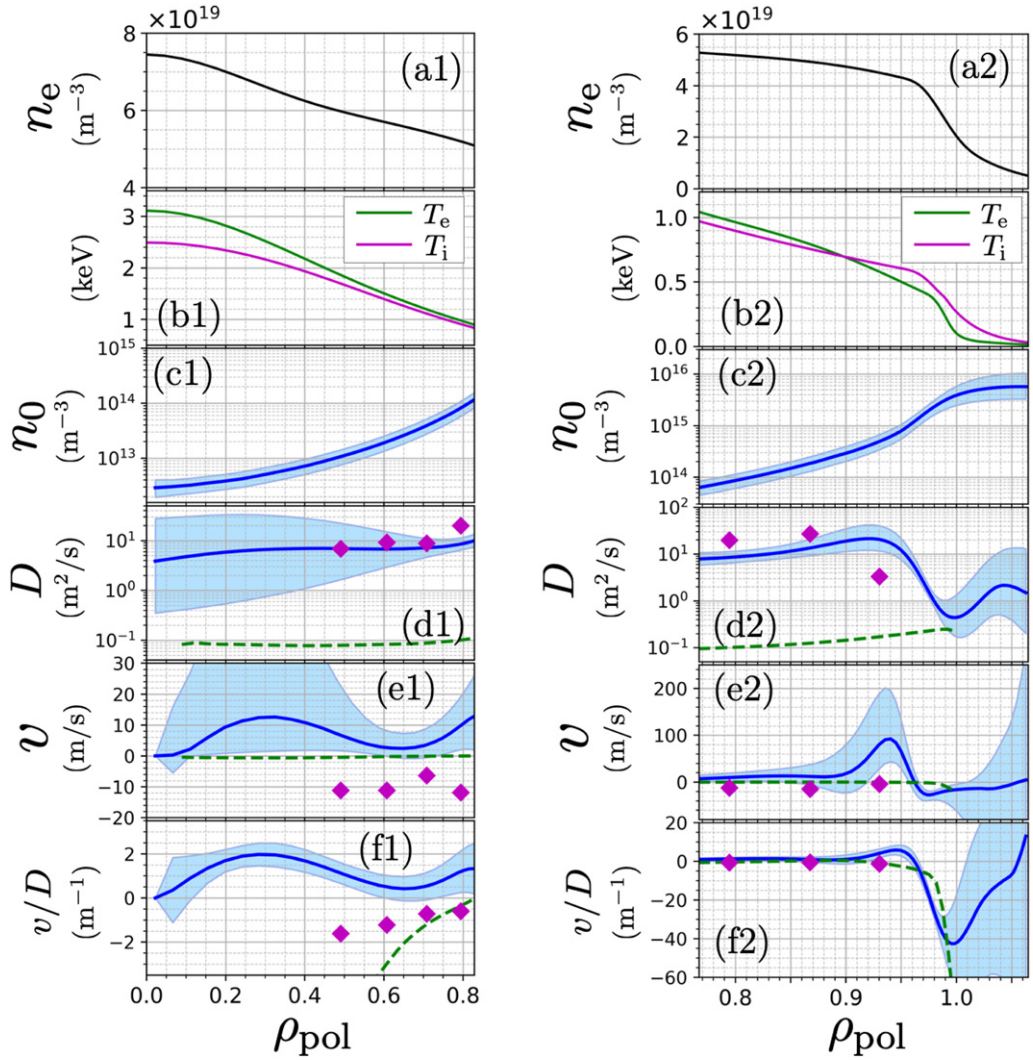


**Figure 3.** Profiles of the electron density: core (*a*1) and edge (*a*2), the electron temperature and the ion temperature: core (*b*1) and edge (*b*2) for a Type-III ELMy H-mode discharge (#38498, time: 7.060–7.075 s). Inferred neutral profile: core (*c*1) and edge (*c*2). Inferred diffusion coefficient profile: core (*d*1) and edge (*d*2). Inferred convection velocity profile: core (*e*1) and edge (*e*2). Inferred profile of the convection-velocity-to-diffusion-coefficient ratio: core (*f* 1) and edge (*f* 2). The blue shaded areas represent the ranges between the 16th and 84th percentiles at each radial point. The blue solid lines show the 50th percentiles at each radial point. The green dashed lines are the neoclassical prediction calculated by neoclassical code (NEO) while the purple diamonds are given by the quasi-linear gyro-fluid code (TGLF-SAT2). The number of samples and autocorrelation are 39 000 and <200 samples, respectively.

equation (B.15) is solved. Thus, somewhat arbitrary choices for the boundary conditions can be tolerated.

Finally, our prior distribution is given by:

$$\begin{aligned} &p(\vec{D},\vec{v},\vec{n}_{\mathrm{C}},\vec{n}_{\mathrm{O}},\vec{n}_{\mathrm{Ne}},\vec{n}_0,\vec{T}_0|\vec{I}_{\mathrm{all}}) \\ &\quad\propto p(\vec{n}_{\mathrm{C}}|\vec{D},\vec{v},\vec{n}_0,\vec{T}_0,\bar{n}_{\mathrm{C}^{6+}})p(\vec{n}_{\mathrm{O}}|\vec{D},\vec{v},\vec{n}_0,\vec{T}_0,\bar{n}_{\mathrm{O}^{8+}}) \\ &\quad\times p(\vec{n}_{\mathrm{Ne}}|\vec{D},\vec{v},\vec{n}_0,\vec{T}_0,\bar{n}_{\mathrm{Ne}^{10+}}) \\ &\quad\times p(\vec{v}|\hat{\Omega},\vec{D})p(\vec{D}|\hat{\Sigma})p(\vec{n}_0,\vec{T}_0|E_{0,\mathrm{wall}},n_{0,\mathrm{wall}}) \\ &\quad\times p(\bar{n}_{\mathrm{C}^{6+}})p(\bar{n}_{\mathrm{O}^{8+}})p(\bar{n}_{\mathrm{Ne}^{10+}})p(E_{0,\mathrm{wall}})p(n_{0,\mathrm{wall}}), \end{aligned} \tag{13}$$

where $\vec{I}_{\mathrm{all}}$ represents all the prior beliefs contained on the rhs. We use logarithmic priors for $p(\bar{n}_{\mathrm{C}^{6+}})$, $p(\bar{n}_{\mathrm{O}^{8+}})$, and $p(\bar{n}_{\mathrm{Ne}^{10+}})$.

### 3.4. Likelihood

We calculate the CX emission intensities for given impurity density distributions by using equation (1). The impurity density $n_z$ is given by the prior equation (13), and $\nu_z^\lambda$ can be calculated by using COLRAD. The main consideration in defining the likelihood is to take uncertainties into account. In this paper, we neglect uncertainties in the $\nu_z^\lambda$, $n_e$, $T_e$, and $T_i$ profiles and the atomic data. If these parameters are not fixed, the prior given by equation (13) needs to be modified, and calculating the posterior distribution becomes challenging. Note that since the decoupling of $D$ and $v$ depends solely on the charge state balance in this analysis, the inference results can be more susceptible to the atomic data compared with the conventional approaches. Characterizing this dependency remains future work. The NBI modeling using COLRAD has already

been validated against experimental data [32]. We determine the most probable $n_e$, $T_e$, and $T_i$ profiles through IDA [18], which utilizes multiple diagnostics. Due to the long time-averaging of the CX emission data (over 15 ms), the photon noise has insignificant contributions. Hence, we model correlated and uncorrelated systematic uncertainties within the Bayesian framework.

One of the sources of the correlated uncertainties originates from the darkening of lenses in the optical heads. Access to the inside of the vacuum vessel is limited during an experimental campaign of AUG, which usually lasts around 7 months. We use the calibration data that were taken prior to the experimental campaign. Therefore, some degree of degradation in the transmission was expected when the measurement was carried out. It is expected that the LOSs that share the same optical head are affected by this effect in a similar fashion. In addition, the transmission of the optical heads and the sensitivities of the spectrometers were calibrated individually by using an integrating sphere. There could be different systematic errors when optical systems were irradiated, which also lead to correlated systematic uncertainties. We take into account these uncertainties by forward-modeling CX emission intensities as follows:

$$L^{\mathrm{model}}_{524,j} = \zeta_{k(524,j)}\eta_{l(524,j)}\int_{\mathrm{los}(524,j)} n_{\mathrm{Ne}^{10+}}\nu^{524}_{\mathrm{Ne}^{10+}}\,\mathrm{d}s, \tag{14}$$

$$L^{\mathrm{model}}_{529,j} = \zeta_{k(529,j)}\eta_{l(529,j)}\int_{\mathrm{los}(529,j)} n_{\mathrm{C}^{6+}}\nu^{529}_{\mathrm{C}^{6+}}\,\mathrm{d}s, \tag{15}$$

$$L^{\mathrm{model}}_{607,j} = \zeta_{k(607,j)}\eta_{l(607,j)}\int_{\mathrm{los}(607,j)} (n_{\mathrm{Ne}^{8+}} + n_{\mathrm{O}^{8+}})\nu^{607}_{\mathrm{Ne}^{8+}}\,\mathrm{d}s, \tag{16}$$

where $\zeta_k$ and $\eta_l$ model the uncertainties in the absolute intensity calibration due to the optical heads and due to the spectrometers, respectively. The subscript $k =$ A, B, C represents the optical heads, and the subscript $l =$ CER, CMR, CAR, CPR is for the spectrometers. $k$ and $l$ depend on the wavelength of an emission line $\lambda = 524$, 529, and 607 nm and a LOS $j$. We estimate that the absolute intensity calibration of the optical heads and that of the spectrometers have an uncertainty of 10%. This uncertainty can be implemented by using $\mathcal{N}(1, 0.1^2)$ for the probability distribution of $\zeta_k(\lambda, j)$ and $\eta_k(\lambda, j)$ where $\mathcal{N}(\mu, \sigma^2)$ is a normal distribution with a mean of $\mu$ and a variance of $\sigma^2$.

The main source of uncorrelated uncertainties is an optical fiber coupler. The fibers housed in an optical head are connected to couplers on a fiber adapter panel. Depending on the needs of experiments, the connections between the LOSs and the spectrometers are configured differently. It is known that the transmission of a fiber coupler differs slightly each time, when a fiber is removed and reconnected. We estimate that this process leads to a 10 % error, which has no correlation between the spatial channels. Another source of uncorrelated uncertainties is the subtraction of the base line and passive emission intensities. We assume that this leads to the error of $\epsilon = 10^{14}$ photons/(m$^2$ s sr), which is non-negligible only for 529 nm and 607 nm line measurements in the core region.

Based on the considerations above, we introduce the following likelihood:

$$p(\vec{L}_{524}, \vec{L}_{529}, \vec{L}_{606}|\vec{n}_{\mathrm{C}}, \vec{n}_{\mathrm{O}}, \vec{n}_{\mathrm{Ne}}) \propto \prod_{\lambda,j}\exp\left(-\frac{(L_{\lambda,j} - L^{\mathrm{model}}_{\lambda,j})^2}{2(0.1L^{\mathrm{model}}_{\lambda,j} + \epsilon)^2}\right), \tag{17}$$

where $L^{\mathrm{model}}_{\lambda,j}$ is given by equations (14)–(16).

### 3.5. Markov chain Monte Carlo method

We numerically calculate the posterior probability distribution by using a Markov chain Monte Carlo (MCMC) method [38]. In our model, the probability distributions of equations (7) and (10) have the same number of degrees of freedom as that of the spatial grid points. Since the computation rapidly becomes more expensive as the dimensionality increases, an efficient MCMC algorithm is necessary in this inference problem. We employ No-U-Turn Sampler algorithm [25], which has a favorable scaling property for dimensionality compared with other MCMC algorithms, such as random-walk Metropolis [25, 39, 40].

Due to the complexity of the model, Markov chains often get trapped at local maxima before they reach a typical set when the likelihood equation (17) is evaluated in its original form. In order to facilitate the MCMC sampling, we rewrite equation (17) in the asymptotic form [27]:

$$\breve{p}(\vec{L}_{524}, \vec{L}_{529}, \vec{L}_{606}|\vec{n}_{\mathrm{C}}, \vec{n}_{\mathrm{O}}, \vec{n}_{\mathrm{Ne}}) \propto \prod_{\lambda,j}\exp\left(-\frac{|z(\lambda,j)|^2}{2}\cdot\frac{1 + uv^2|z(\lambda,j)|}{1 + v^2|z(\lambda,j)|^2/2}\right), \tag{18}$$

where

$$z(\lambda, j) = \frac{L_{\lambda,j} - L^{\mathrm{model}}_{\lambda,j}}{0.1L^{\mathrm{model}}_{\lambda,j} + \epsilon}, \tag{19}$$

$u = 1$, and $v = 0.2$. This asymptotic form simplifies the probability distribution in the volume where the probability is extremely low while $\breve{p}(\vec{L}_{524}, \vec{L}_{529}, \vec{L}_{606}|\vec{n}_{\mathrm{C}}, \vec{n}_{\mathrm{O}}, \vec{n}_{\mathrm{Ne}}) \approx p(\vec{L}_{524}, \vec{L}_{529}, \vec{L}_{606}|\vec{n}_{\mathrm{C}}, \vec{n}_{\mathrm{O}}, \vec{n}_{\mathrm{Ne}})$ holds in the typical set. Markov chains robustly reach and explore the typical set when equation (18) is used for the likelihood. The MCMC computation for this model took <400 h to obtain around 200 independent samples by using an Apple M1 chip.

## 4. Results of impurity transport coefficient inference

We have defined the prior equation (13) and the likelihood equation (17) in section 3. Using these probability distributions, the posterior is given by:

$$p(\vec{D}, \vec{v}, \vec{n}_{\mathrm{C}}, \vec{n}_{\mathrm{O}}, \vec{n}_{\mathrm{Ne}}, \vec{n}_0, \vec{T}_0|\vec{L}_{524}, \vec{L}_{529}, \vec{L}_{606}, \vec{I}_{\mathrm{all}}) \propto p(\vec{L}_{524}, \vec{L}_{529}, \vec{L}_{606}|\vec{n}_{\mathrm{C}}, \vec{n}_{\mathrm{O}}, \vec{n}_{\mathrm{Ne}}) \times p(\vec{D}, \vec{v}, \vec{n}_{\mathrm{C}}, \vec{n}_{\mathrm{O}}, \vec{n}_{\mathrm{Ne}}, \vec{n}_0, \vec{T}_0|\vec{I}_{\mathrm{all}}). \tag{20}$$

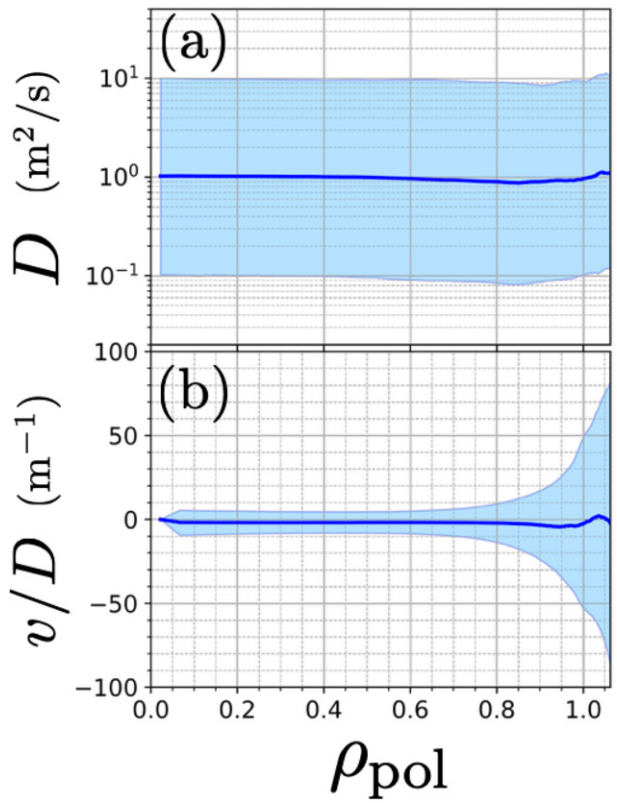


**Figure 4.** Profiles of the diffusion coefficient ($a$) and the convection-velocity-to-diffusion-coefficient ratio calculated by marginalizing the prior equation (13). The blue shaded areas represent the ranges between the 16th and 84th percentiles at each radial point. The blue solid lines show the 50th percentiles at each radial point. The number of samples and autocorrelation are 40 000 and <200 samples, respectively.

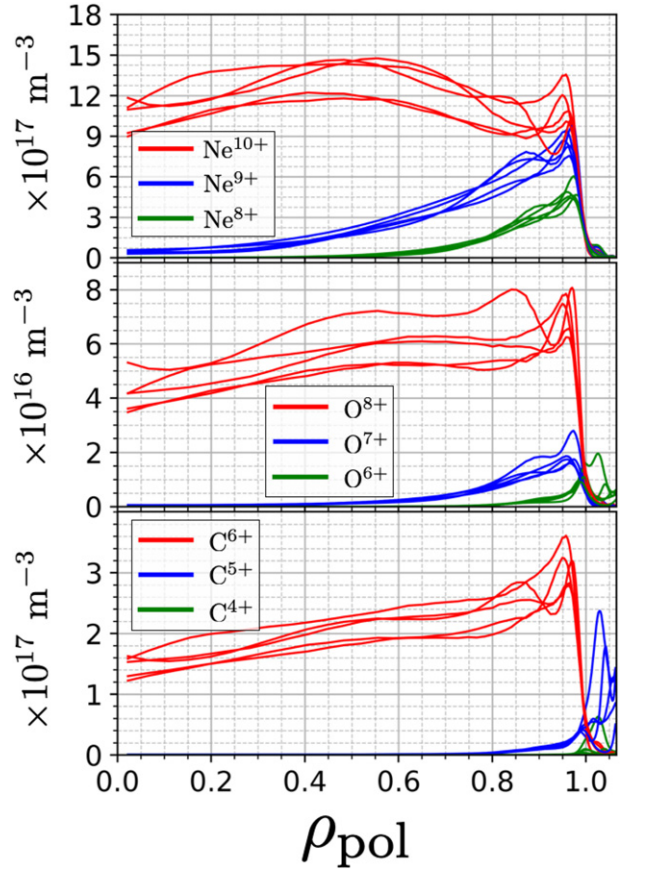


**Figure 5.** Examples of the impurity profiles taken from the posterior distribution.

We calculate the posterior distribution using MCMC, the details of which are already discussed in section 3.5. The probability distribution of one plasma parameter profile can be obtained by marginalizing other parameters. For example, the probability distribution of the $D$ profile is

$$p(\vec{D}|\vec{L}_{524},\vec{L}_{529},\vec{L}_{606},\vec{I}_{\rm all}) = \int p(\vec{D},\vec{v},\vec{n}_{\rm C},\vec{n}_{\rm O},\vec{n}_{\rm Ne},\vec{n}_0,\vec{T}_0|\vec{L}_{524},\vec{L}_{529},\vec{L}_{606},\vec{I}_{\rm all}) \times {\rm d}\vec{v}\,{\rm d}\vec{n}_{\rm C}\,{\rm d}\vec{n}_{\rm O}\,{\rm d}\vec{n}_{\rm Ne}\,{\rm d}\vec{n}_0\,{\rm d}\vec{T}_0. \quad (21)$$

The marginalized posterior distributions of the transport coefficients and the neutral profile for the type-III ELMy H-mode discharge are shown in figure 3 together with the $n_{\rm e}$, $T_{\rm e}$, and $T_{\rm i}$ profiles, which are treated as known parameters. The inferred neutral profiles are similar to the ones for the type-I ELM cases reported in reference [30]. Without taking into account the CX reactions with the thermal neutrals, the forward model is not able to reproduce the Ne X and Ne VIII intensities, which is already pointed out in reference [30]. The $D$ and $v$ profiles for neon calculated by a NEO and a quasi-linear gyro-fluid code (TGLF SAT-2) [11, 17] are also plotted for comparison. Fast ions are neglected in both calculations while electromagnetic terms are included in the TGLF modeling. In the pedestal, the diffusion coefficient $D$ is below one, being close to the neoclassical level provided by NEO. The inferred $v/D$ profile indicates that an inward pinch exists in this region. These observations are in a qualitative agreement with the $D$ and $v$ measurements of type-I ELMy H-mode discharges [8, 15, 30]. Just inside the pedestal top $\rho_{\rm pol} = 0.9$–$0.95$, the diffusion coefficient peaks around $D = 20\,{\rm m}^2\,{\rm s}^{-1}$, and a strong outward convection $\sim$100 m s$^{-1}$ is seen. Neither NEO or TGLF modeling predicts such a magnitude of convection. The Type-III ELM crashes, which are included in the CXRS measurements but not in the NEO and TGLF calculations, may contribute to this discrepancy. Since the Type-III ELM consisted of major crashes with the frequency of around 200 Hz and minor crashes with higher frequencies, filtering out ELMs was difficult by using the current CXRS system.

The posterior is proportional to the product of the likelihood and the prior. Therefore, it is important to inspect how much the likelihood updates the prior distribution. The profiles of $D$ and $v/D$ calculated by running MCMC without the likelihood are shown in figure 4. The prior distribution of $\vec{D}$ given by equation (7) should produce the distribution with the mean of 1 and the standard deviation of a factor of 10 over all radial positions, which is shown in figure 4($a$) as expected. Small deviations are due to the statical uncertainties in the MCMC sampling. Since we allocated shorter correlation lengths $l_{\rm co}$ in the edge, the prior leads to a wider distribution of $v/D$ as $\rho_{\rm pol}$ increases. The inferred $D$ distribution in

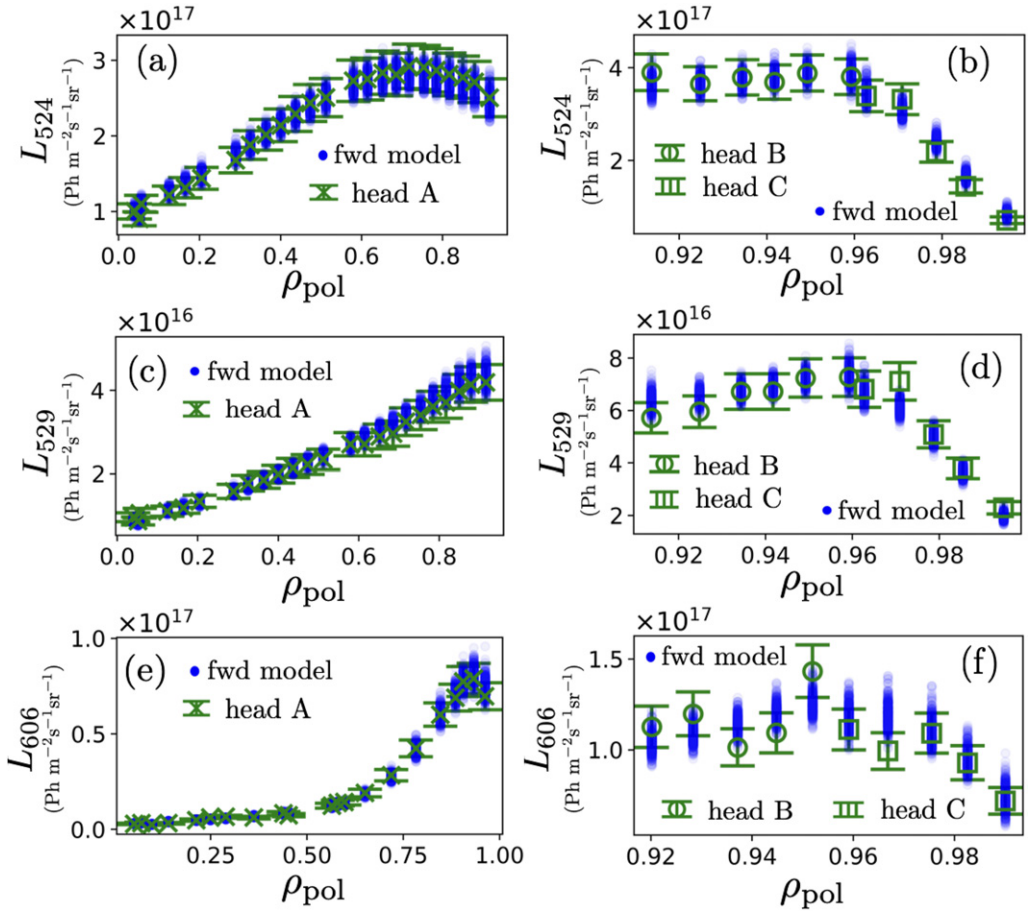


**Figure 6.** Charge exchange emission intensities and forward-model data points. (*a*) and (*c*) are for CER while (*b*) and (*d*) are for CMR. (*e*) and (*f*) are for CAR and CPR, respectively. The shapes of the green markers represent the optical heads used for the measurements. The blue points are forward-modeled data points corresponding to the posterior distributions. Their explicit expressions are given by equations (14)–(16).

figures 3(*d*1) and (*d*2) becomes close to figure 4(*a*) in the core and outside the LCFS, indicating that the likelihood does not provide much constraints in those regions. The profiles of three highest charge states for neon, oxygen and carbon randomly taken from the posterior distribution are shown in figure 5. In the core $\rho_{\rm pol} < 0.4$, the profiles of the highest charge states are almost the same as those of the sum of all charge states for all impurity species. In this region we cannot decouple $v$ and $D$, and only the ratio of $v$ to $D$ can be inferred. The probability distributions of $v/D$ shown in figures 3($f$1) and ($f$2) are more localized compared with the distribution shown figure 4(*b*), indicating that the distribution is updated by the likelihood. $v/D \sim 0.5$–$2.0$ m$^{-1}$ in the core inferred from the CXRS measurements produces slightly hollow impurity profiles as shown in figure 5 while the NEO and TGFL modeling predicts inward convections and the resultant peaked impurity profiles in this region. The broad probability distributions of $D$ and $v/D$ outside the LCFS is expected since no CXRS measurements are available there. While the large uncertainties in the transport properties exist in the SOL, the probability distributions become localized sharply once they move into the confined region.

The consistency between the assumed systematic uncertainties and the CXRS measurements can be examined by using the forward-modeled data. Figure 6 shows the CX intensities and the forward-modeled data points corresponding to the posterior distribution. Reasonable agreements are seen over all channels, indicating that the likelihood given by equation (17) is appropriate. Note that impurity profiles shown in figure 5 have rather large variations in shape, but they all reproduce the CXRS data reasonably well as shown in figure 6. Unlike the standard fitting technique, the analysis framework presented in this paper takes into account all possible impurity profiles that satisfy the prescribed line properties given by the prior.

## 5. Conclusions

In this paper, we have introduced a non-parametric inference framework for the impurity coefficient measurements. The input data are the intensities of Ne X, Ne VIII, O VIII, and C VI lines measured by CXRS. Unlike conventional methods that use transient impurity profiles to decouple the diffusion coefficient $D$ and the convection velocity $v$, we utilize a

quasi-stationary plasma. The ratio of $v$ to $D$ only describes the equilibrated profile of the sum of all charge states, and spatial variations of each charge state depend on both $D$ and $v$, not on $v/D$. Thus, if one impurity species has significant populations in multiple charge states, $D$ and $v$ can still be separated by simultaneously observing more than one charge state.

We have formulated the analysis framework based on the Bayesian probability theory, which allows for the coherent integration of data and the systematic uncertainty estimations. Instead of introducing specific functions for the profiles of $D$ and $v$, we employ a non-parametric approach, which does not reduce the degrees of freedom for representing the profiles. Therefore, the posterior distribution contains all possible solutions that are consistent with the measurements and the smoothness conditions given by the prior beliefs. The parametrization of the transport coefficients and other parameters necessary for constructing the model is chosen such that it facilitates the use of MCMC sampling. The impurity profiles in a steady state for a given set of $D$ and $v$ are determined analytically, and the posterior distribution defined in a nearly 200 dimensional space has been calculated. In addition, systematic uncertainties, which are typically difficult to address in the conventional fitting procedure, are embedded in the likelihood distribution within the Bayesian framework. The forward model also takes into account the charge exchange reactions with the background thermal neutrals in the confined region. While posing an additional challenge in the inference problem, addressing this effect is necessary to properly model the charge state balance of impurity ions.

We have inferred the profiles of impurity transport coefficients of neon, oxygen and carbon for a Type-III ELMy H-mode plasma at ASDEX Upgrade by assuming that these three impurity species have the same transport properties. The forward modeled data points corresponding to the posterior are in reasonable agreements with the CXRS measurements. In the edge region where $Ne^{8+}$ ions have a significant population, $D$ and $v$ are clearly separated. $D$ varies from $\sim$0.5 to $\sim$20 m s$^{-2}$ from the pedestal region to the inside of the pedestal top. A strong outward convection $v \sim 100$ m s$^{-1}$ is also observed right inside the pedestal top. All measured impurity species are almost fully ionized in the core, and the inferred $D$ profile becomes close to the distribution given by the prior alone. In this region, a meaningful inference is possible only for $v/D$.

The analysis framework discussed in this paper is applicable to other impurity species. Currently, argon charge exchange measurements are being developed at AUG [41]. Due to its higher atomic number, argon impurities have significant populations in lower charge states even in the core of the AUG plasmas. Therefore, we will be able to separate $D$ and $v$ over the whole radial position if argon charge exchange emissions are measured. Furthermore, integrating other diagnostics, e.g. soft x-ray and vacuum ultraviolet spectroscopy and bolometry, within the Bayesian framework will further improve the inference of impurity transport coefficients.

## Acknowledgments

This work has been carried out within the framework of the EUROfusion Consortium and has received funding from the Euratom research and training programme 2014–2018 and 2019–2020 under Grant Agreement No. 633053. The views and opinions expressed herein do not necessarily reflect those of the European Commission.

## Appendix A. Parametric vs non-parametric profile inference in the Bayesian framework

We briefly review the parametric and non-parametric profile inferences in the Bayesian framework. Firstly, we consider a general case where $\vec{r}^{\mathsf{T}} = [r_1, r_2, \ldots, r_N]$ are the discretized radial points, and $\vec{\theta}^{\mathsf{T}} = [\theta_1, \theta_2, \ldots, \theta_N]$ are the radial profile of some plasma parameter. Then, we visualize probability distributions for each profile inference approach by using a low dimensional example.

When $\vec{d}$ is an available data set, Bayes' theorem gives the posterior distribution as follows:

$$p(\vec{\theta}|\vec{d}, \vec{I}) \propto p(\vec{d}|\vec{\theta}, \vec{I}) p(\vec{\theta}|\vec{I}), \tag{A.1}$$

where $\vec{I}$ is the prior brief, which represents what we know about the system, or what we assume before measurements are taken. The prior distribution $p(\vec{\theta}|\vec{I})$ gives the probability distribution of the $\theta$ profile based only on our prior belief. It is not straight-forward to define a prior that contains only sensible profiles. For example, when we use uniform distributions for $\theta$ at all radial points, the prior is

$$\begin{aligned} p(\vec{\theta}|\vec{I}) = {} & U(\theta_{1,\min}, \theta_{1,\max}) U(\theta_{2,\min}, \theta_{2,\max}) \\ & \ldots U(\theta_{N,\min}, \theta_{N,\max}), \end{aligned} \tag{A.2}$$

where $U(\theta_{n,\min}, \theta_{n,\max})$ is a uniform distribution ranging from $\theta_{n,\min}$ to $\theta_{n,\max}$. In this case, $p(\vec{\theta}|\vec{I})$ is defined in an $N$ dimensional space. When a point in that high dimensional space is within the upper and lower limits for all dimensions, it always has the same probability. If we randomly draw samples from this distribution, most of them will be non-sensible profiles, which lack smoothness. While the posterior distribution is given by the product of the prior and the likelihood, the likelihood alone typically fails to exclude unphysical profiles since the number of constraints provided by measurements is usually smaller than the number of the required spatial grid points, i.e., the problem is ill-posed. Therefore, we need to implement some type of smoothness conditions in the prior and remove non-sensible profiles from the posterior for realistic diagnostic setups. This can be achieved by either parametric or non-parametric approach.

First, we consider a parametric profile inference. We let $\vec{I}$ have the belief that $\theta_n = f(r_n, \vec{x})$, where $f$ is a function with undetermined parameters:$\vec{x}^{\mathsf{T}} = [x_1, x_2, \ldots, x_M]$. They correspond to the fitting parameters in the conventional fitting procedure. Here, $M < N$. Using $f$, the prior is given by:

$$p(\vec{\theta}|\vec{I}) \propto \prod_{n=1}^{N} \delta(\theta_n - f(r_n, \vec{x}))p(\vec{x}|\vec{I}), \tag{A.3}$$

where $\delta(\ldots)$ is a delta function, which takes a non-zero value only when $\theta_n - f(r_n, \vec{x})$ is zero. The prior equation (A.3) has finite probabilities only for $\vec{\theta}$ that can be represented by a function $f$.

Next, we discuss a non-parametric profile inference. In this case, we directly assign probabilities to $\vec{\theta}$ without introducing a specific functional model. While there are many techniques to achieve this, we limit ourselves to the non-parametric profile inference based on the Gaussian process. When we employ the Gaussian process, the prior distribution is given by:

$$p(\vec{\theta}|\vec{I}) = p(\vec{\theta}|\vec{\mu},\ \hat{\Sigma}) \propto \exp\left(-\frac{1}{2}(\vec{\theta} - \vec{\mu})^{\intercal}\hat{\Sigma}^{-1}(\vec{\theta} - \vec{\mu})\right), \tag{A.4}$$

where $\vec{\mu}$ and $\hat{\Sigma}$ are a mean vector and a covariance matrix, respectively. The prior beliefs such as smoothness conditions can be implemented in those quantities. $\vec{\mu}$ and $\hat{\Sigma}$ are called hyper-parameters, which play a different role than $\vec{x}$ since they are used to define the probability distribution of $\vec{\theta}$ without reducing the dimension of its original parameter space.

In order to obtain the intuitive understanding of the parametric and non-parametric profile inferences, we consider a simple case where there are only three spatial points $\vec{r}^{\intercal} = [1, 2, 3]$ as shown in figure A1($a$). We assume that the measurements lead to the likelihood shown in figure A1($b$). Due to the insufficient constraints, the maximum likelihood is not a point, but a line. Therefore, we cannot find a single optimum point based on the likelihood alone. In addition, the high probability volume contains non-smooth profiles. For the parametric approach, we use a linear function:

$$\theta_n = x_1 r_n + x_2. \tag{A.5}$$

The prior distribution for this function is shown in figure A2($a$). We employ uniform distributions for $p(x_1)$ and $p(x_1)$. Since we have only two parameters to describe three spatial points, the prior distribution spans on a two-dimensional surface defined in the three dimensional space. While the probability is the same on the surface in this specific parametrization, there are generally variations in probability on the surface or in the volume that a model function defines. As for the non-parametric inference, we use a squared exponential covariance matrix:

$$\Sigma_{n,n'} = \sigma^2 \exp\left(-\frac{(r_n - r_{n'})^2}{2l^2}\right), \tag{A.6}$$

where $\sigma = 1$, $l = 2$. We choose $\vec{\mu} = \vec{0}$ for the mean vector in equation (A.4). The prior distribution given by the Gaussian process is shown in figure A2($b$). The probability is high near the surface corresponding to linear profiles. However, the prior has a three-dimensional distribution unlike figure A1($a$). As Bayes' theorem equation (A.1) states, the posterior distribution is given by multiplying the prior figure A2($a$) or ($b$) by the likelihood figure A1($b$). Figures A2($c$) and ($d$) show the posterior distributions for the parametric and non-parametric

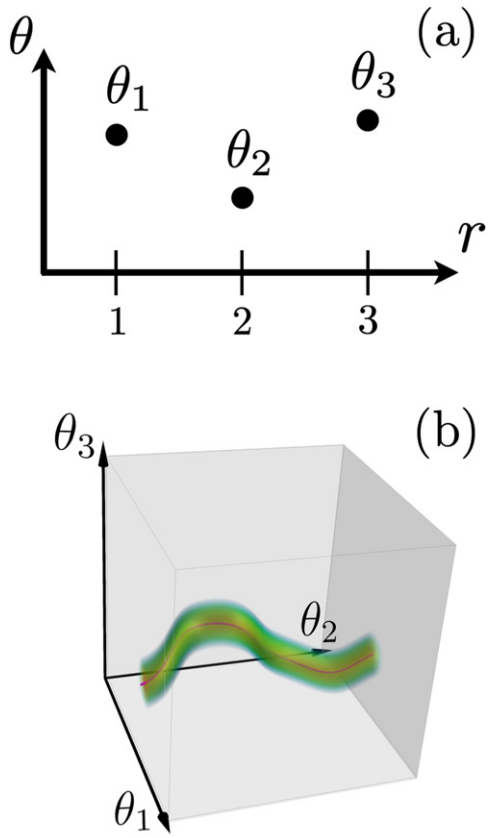


**Figure A1.** Relation between $r_n$ and $\theta_n$ ($a$) and an example of the likelihood that leads to an ill-posed inference problem ($b$).

inferences, respectively. In the parametric inference, the posterior does not contain any points that are not on the surface defined by the prior even though the volume near the surface represents rather smooth profiles. On the other hand, the non-parametric inference provides the posterior distribution whose degrees of freedom are the same as the number of spatial points. Even for non-straight profiles, the posterior shown in figure A2($d$) has high probabilities as long as they have reasonable smoothness. The relative importance between the likelihood and the smoothness conditions is controlled by the hyper parameters.

When inferring plasma parameter profiles from experimental data, much larger numbers of spatial points are required. In such a case, a further reduction in the degrees of freedom is expected in the parametric approach. Furthermore, the volume defined by the model function does not necessarily overlap the high probability regions in the likelihood. While complex functions are more likely to contain the high likelihood regions, profiles with non-sensible structures may also be included in the posterior distributions. The Bayes factor [9, 11] is often used for optimizing the function model. The non-parametric approach preserves the degrees of freedom even when many more spatial grid points are used for representing spatial profiles. Since the true plasma parameter profiles are reasonably smooth, the posterior contains the high probability regions in the likelihood unless the smoothness condition is too strong. While criteria exist for the hyper-parameter optimization [42], they require unpractically large

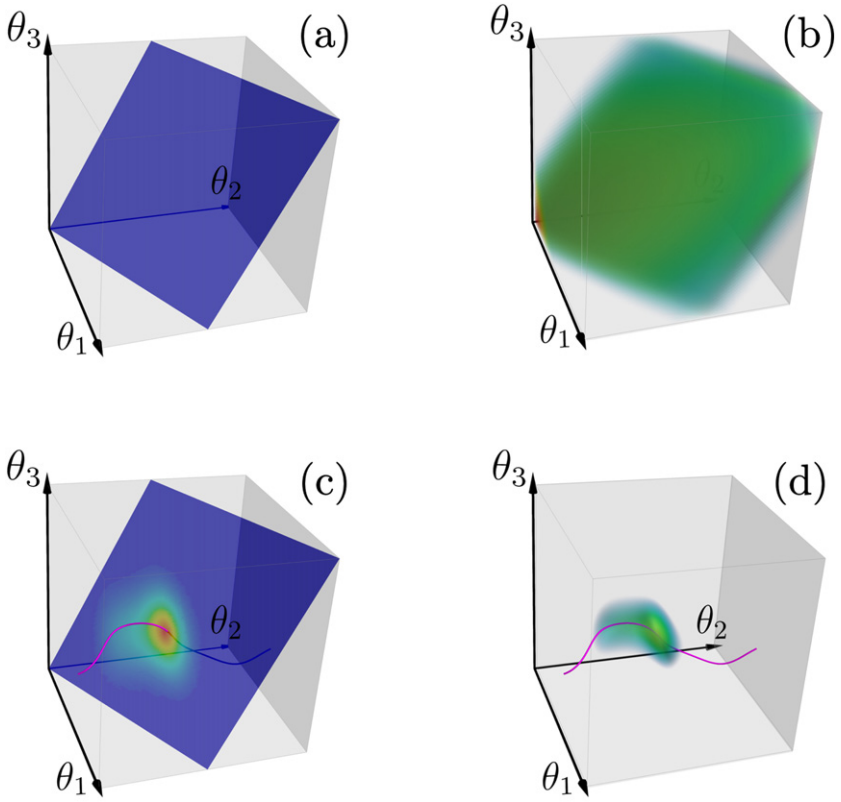


**Figure A2.** Prior distributions for a parametric approach (*a*) and a non-parametric approach (*b*). Posterior distributions for a parametric approach (*c*) and a non-parametric approach (*d*). The line of the maximum likelihood is shown by the purple line. Each axis shown in these plots spans from 0 to 1.

amounts of computation for the inference problem discussed in this paper. Therefore, we use fixed hyper parameters. In the non-parametric profile inference, all solutions with the smoothness prescribed by the prior are contained in the posterior distribution.

## Appendix B. Analytical solution for impurity profiles in a steady state

We consider an impurity species with the atomic number of $Z$. A particle balance for a charge state $z(\leqslant Z)$ in a cylindrical coordinate system is given by:

$$\frac{\partial n_z}{\partial t} = \frac{1}{r}\frac{\partial}{\partial r} r\left(D\frac{\partial n_z}{\partial r} - v n_z\right) + s_z, \tag{B.1}$$

where $s_z$ is the source term, and the definitions of other quantities are the same as the ones already given in this paper. When the system is stationary, e.g., all quantities are independent of $t$, the following equation holds:

$$\frac{\mathrm{d}}{\mathrm{d}r} r\left(D\frac{\mathrm{d}n_z}{\mathrm{d}r} - v n_z\right) = -r s_z. \tag{B.2}$$

This leads to

$$\frac{\mathrm{d}n_z}{\mathrm{d}r} - \frac{v}{D} n_z = -\frac{1}{Dr}\int_0^r \mathrm{d}r'\, s_z(r') r' + \frac{C}{Dr}, \tag{B.3}$$

where $C$ is a constant. At $r = 0$, $\mathrm{d}n_z/\mathrm{d}r = 0$, and $v = 0$ due to the cylindrical geometry. Thus, $C = 0$. By solving for $n_z$, we have

$$\begin{aligned} n_z(r) = \exp\left(-\int_r^{r_{\mathrm{edge}}} \mathrm{d}r' \frac{v(r')}{D(r')}\right) \Bigg[\int_r^{r_{\mathrm{edge}}} \frac{\mathrm{d}r'}{D(r')r'} \\ \times \exp\left(\int_{r'}^{r_{\mathrm{edge}}} \frac{v(r'')}{D(r'')}\mathrm{d}r''\right) \\ \times \int_0^{r'} \mathrm{d}r'' s_z(r'') r'' + n_z(r_{\mathrm{edge}})\Bigg], \end{aligned} \tag{B.4}$$

where $r_{\mathrm{edge}}$ is the outermost radial point in the system. The densities of all charge states need to be specified there. We found that the overall profile shapes in the confined region for given background plasma parameters and impurity transport coefficients are relatively insensitive to the boundary conditions at the edge. In contrast, small changes in the charge state balance in the core lead to large differences in the resulting profiles. Therefore, we choose to define boundary conditions at the edge.

When $z \neq Z, 1$, the source $s_z$ arises through recombination and ionization, which involve the interaction with $n_{z-1}$ and $n_{z+1}$, namely

$$\begin{aligned} s_z(r) = &+a_{z+1}(r)n_{z+1}(r) - b_z(r)n_z(r) \\ &- a_z(r)n_z(r) + b_{z-1}(r)n_{z-1}(r), \end{aligned} \tag{B.5}$$

where $a_z$ and $b_z$ specify recombination and ionization, respectively. For simplicity, we neglect the parallel loss term in the SOL while it is included in the impurity transport analysis presented in this paper. The parallel loss can be added by following a procedure similar to that of recombination and ionization given below. By plugging equation (B.5) into equation (B.4),

$$\begin{aligned} n_z(r) =& n_z(r_{\mathrm{edge}}) \exp\left(-\int_r^{r_{\mathrm{edge}}} \mathrm{d}r' \frac{v(r')}{D(r')}\right) \\ &+ A_{z+1}n_{z+1}(r'') - B_z n_z(r'') \\ &- A_z n_z(r'') + B_{z-1}n_{z-1}(r''), \end{aligned} \tag{B.6}$$

where

$$\begin{aligned} A_z = &\, \mathrm{e}^{-\int_r^{r_{\mathrm{edge}}} \mathrm{d}r' \frac{v(r')}{D(r')}} \int_r^{r_{\mathrm{edge}}} \mathrm{d}r' \frac{\mathrm{e}^{\int_{r'}^{r_{\mathrm{edge}}} \mathrm{d}r'' \frac{v(r'')}{D(r'')}}}{D(r')r'} \\ &\times \int_0^{r'} \mathrm{d}r'' a_z(r'')r'', \end{aligned} \tag{B.7}$$

$$\begin{aligned} B_z = &\, \mathrm{e}^{-\int_r^{r_{\mathrm{edge}}} \mathrm{d}r' \frac{v(r')}{D(r')}} \int_r^{r_{\mathrm{edge}}} \mathrm{d}r' \frac{\mathrm{e}^{\int_{r'}^{r_{\mathrm{edge}}} \mathrm{d}r'' \frac{v(r'')}{D(r'')}}}{D(r')r'} \\ &\times \int_0^{r'} \mathrm{d}r'' b_z(r'')r''. \end{aligned} \tag{B.8}$$

Note that $r''$ in equation (B.6) is an integration variable. The density of the highest charge state $n_Z$ is given by removing $+A_{z+1}n_{z+1}(r'')$ and $-B_z n_z(r'')$ from equation (B.6) while omitting $-A_z n_z(r'')$ and $+B_{z-1}n_{z-1}(r'')$ leads to $n_1$. We neglect the impurities in the neutral state in this analysis.

Next, we discretize the profiles and use vectors to represent the density profiles of charge states:

$$\vec{n}_z = \begin{bmatrix} n_{z,1} \\ n_{z,2} \\ \vdots \\ n_{z,N} \end{bmatrix}, \tag{B.9}$$

where $n_{z,1}$ and $n_{z,N}$ represent the core and edge densities, respectively. Using this notation,

$$\vec{n}_z = \begin{cases} n_{z,N+1}\vec{u} + \hat{A}_{z+1}\vec{n}_{z+1} - \hat{B}_z\vec{n}_z, & \text{if } z = 1 \\ n_{z,N+1}\vec{u} - \hat{A}_z\vec{n}_z + \hat{B}_{z-1}\vec{n}_{z-1}, & \text{if } z = Z \\ n_{z,N+1}\vec{u} + \hat{A}_{z+1}\vec{n}_{z+1} - (\hat{A}_z + \hat{B}_z)\vec{n}_z + \hat{B}_{z-1}\vec{n}_{z-1}, & \text{otherwise,} \end{cases} \tag{B.10}$$

where

$$\vec{u} = \begin{bmatrix} u_1 \\ u_2 \\ \vdots \\ u_N \end{bmatrix}, \qquad u_i = \exp\left(-\sum_{l=1}^{N+1-i} \frac{v_{N+1-l}}{D_{N+1-l}} \Delta r_{N+1-l}\right), \tag{B.11}$$

$$\begin{aligned} \hat{A}_z = &\begin{bmatrix} u_1 & 0 & \dots & 0 \\ 0 & u_2 & \dots & 0 \\ \vdots & \vdots & \ddots & \vdots \\ 0 & 0 & \dots & u_N \end{bmatrix} \begin{bmatrix} \Delta r_1 & \Delta r_2 & \dots & \Delta r_N \\ 0 & \Delta r_2 & \dots & \vdots \\ \vdots & \vdots & \ddots & \vdots \\ 0 & 0 & \dots & \Delta r_N \end{bmatrix} \\ &\cdot \begin{bmatrix} \frac{1}{u_1 D_1 r_1} & 0 & \dots & 0 \\ 0 & \frac{1}{u_2 D_2 r_2} & \dots & 0 \\ \vdots & \vdots & \ddots & \vdots \\ 0 & 0 & \dots & \frac{1}{u_N D_N r_N} \end{bmatrix} \\ &\cdot \begin{bmatrix} \Delta r_1 & 0 & \dots & 0 \\ \Delta r_1 & \Delta r_2 & \dots & \vdots \\ \vdots & \vdots & \ddots & \vdots \\ \Delta r_1 & \Delta r_2 & \dots & \Delta r_N \end{bmatrix} \\ &\cdot \begin{bmatrix} a_{z,1} r_1 & 0 & \dots & 0 \\ 0 & a_{z,2} r_2 & \dots & 0 \\ \vdots & \vdots & \ddots & \vdots \\ 0 & 0 & \dots & a_{z,N} r_N \end{bmatrix}, \end{aligned} \tag{B.12}$$

$$\begin{aligned} \hat{B}_z = &\begin{bmatrix} u_1 & 0 & \dots & 0 \\ 0 & u_2 & \dots & 0 \\ \vdots & \vdots & \ddots & \vdots \\ 0 & 0 & \dots & u_N \end{bmatrix} \begin{bmatrix} \Delta r_1 & \Delta r_2 & \dots & \Delta r_N \\ 0 & \Delta r_2 & \dots & \vdots \\ \vdots & \vdots & \ddots & \vdots \\ 0 & 0 & \dots & \Delta r_N \end{bmatrix} \\ &\cdot \begin{bmatrix} \frac{1}{u_1 D_1 r_1} & 0 & \dots & 0 \\ 0 & \frac{1}{u_2 D_2 r_2} & \dots & 0 \\ \vdots & \vdots & \ddots & \vdots \\ 0 & 0 & \dots & \frac{1}{u_N D_N r_N} \end{bmatrix} \\ &\cdot \begin{bmatrix} \Delta r_1 & 0 & \dots & 0 \\ \Delta r_1 & \Delta r_2 & \dots & \vdots \\ \vdots & \vdots & \ddots & \vdots \\ \Delta r_1 & \Delta r_2 & \dots & \Delta r_N \end{bmatrix} \\ &\cdot \begin{bmatrix} b_{z,1} r_1 & 0 & \dots & 0 \\ 0 & b_{z,2} r_2 & \dots & 0 \\ \vdots & \vdots & \ddots & \vdots \\ 0 & 0 & \dots & b_{z,N} r_N \end{bmatrix}. \end{aligned} \tag{B.13}$$

Equation (B.10) for different charge states can be combined and written as a linear equation:

$$\begin{bmatrix} \vec{n}_1 \\ \vec{n}_2 \\ \vec{n}_3 \\ \vdots \\ \vec{n}_{Z-1} \\ \vec{n}_Z \end{bmatrix} = \begin{bmatrix} n_{1,N+1}\vec{u} \\ n_{2,N+1}\vec{u} \\ n_{3,N+1}\vec{u} \\ \vdots \\ n_{Z-1,N+1}\vec{u} \\ n_{Z,N+1}\vec{u} \end{bmatrix} + \begin{bmatrix} -\hat{B}_1 & \hat{A}_2 & 0 & 0 & \dots & 0 & 0 & 0 \\ \hat{B}_1 & -\hat{A}_2 - \hat{B}_2 & \hat{A}_3 & 0 & \dots & 0 & 0 & 0 \\ 0 & \hat{B}_2 & -\hat{A}_3 - \hat{B}_3 & \hat{A}_4 & \dots & 0 & 0 & 0 \\ \vdots & \vdots & \vdots & \vdots & \ddots & \vdots & \vdots & \vdots \\ 0 & 0 & 0 & 0 & \dots & \hat{B}_{Z-2} & -\hat{A}_{Z-1} - \hat{B}_{Z-1} & \hat{A}_Z \\ 0 & 0 & 0 & 0 & \dots & 0 & \hat{B}_{Z-1} & -\hat{A}_Z \end{bmatrix} \begin{bmatrix} \vec{n}_1 \\ \vec{n}_2 \\ \vec{n}_3 \\ \vdots \\ \vec{n}_{Z-1} \\ \vec{n}_Z \end{bmatrix}. \tag{B.14}$$

By moving the second term on the RHS in equation (B.14) to the LHS, and by multiplying both sides by the inverse matrix, an analytical solution for charge state profiles for given $D$ and $v$ is given by:

$$\begin{bmatrix} \vec{n}_1 \\ \vec{n}_2 \\ \vec{n}_3 \\ \vdots \\ \vec{n}_{Z-1} \\ \vec{n}_Z \end{bmatrix} = \hat{M}^{-1} \begin{bmatrix} n_{1,N+1}\vec{u} \\ n_{2,N+1}\vec{u} \\ n_{3,N+1}\vec{u} \\ \vdots \\ n_{Z-1,N+1}\vec{u} \\ n_{Z,N+1}\vec{u} \end{bmatrix} \tag{B.15}$$

where

$$\hat{M} = \begin{bmatrix} \hat{1} + \hat{B}_1 & -\hat{A}_2 & 0 & 0 & \dots & 0 & 0 & 0 \\ -\hat{B}_1 & \hat{1} + \hat{A}_2 + \hat{B}_2 & -\hat{A}_3 & 0 & \dots & 0 & 0 & 0 \\ 0 & -\hat{B}_2 & \hat{1} + \hat{A}_3 + \hat{B}_3 & -\hat{A}_4 & \dots & 0 & 0 & 0 \\ \vdots & \vdots & \vdots & \vdots & \ddots & \vdots & \vdots & \vdots \\ 0 & 0 & 0 & 0 & \dots & \hat{B}_{Z-2} & \hat{1} + \hat{A}_{Z-1} + \hat{B}_{Z-1} & -\hat{A}_Z \\ 0 & 0 & 0 & 0 & \dots & 0 & -\hat{B}_{Z-1} & \hat{1} + \hat{A}_Z \end{bmatrix}. \tag{B.16}$$

Here, $\hat{1}$ is an identity matrix. The validity of equations (B.15) and (B.16) are confirmed by comparing the impurity profiles calculated by STRAHL.

## ORCID iDs

T. Nishizawa https://orcid.org/0000-0003-1804-2308
R.M. McDermott https://orcid.org/0000-0002-8958-8714
C. Schuster https://orcid.org/0000-0002-6695-3336
D.J. Cruz-Zabala https://orcid.org/0000-0001-5925-5153
P. Cano-Megias https://orcid.org/0000-0001-5182-6513

## References

[1] Kallenbach A. *et al* 2013 Impurity seeding for tokamak power exhaust: from present devices via ITER to demo *Plasma Phys. Control. Fusion* **55** 124041
[2] Kallenbach A. *et al* 2020 Developments towards an ELM-free pedestal radiative cooling scenario using noble gas seeding in ASDEX Upgrade *Nucl. Fusion* **61** 016002
[3] McKee G., Burrell K., Fonck R., Jackson G., Murakami M., Staebler G., Thomas D. and West P. 2000 Impurity-induced suppression of core turbulence and transport in the DIII-D tokamak *Phys. Rev. Lett.* **84** 1922–5
[4] Osakabe M. *et al* 2014 Impact of carbon impurities on the confinement of high-ion-temperature discharges in the large helical device *Plasma Phys. Control. Fusion* **56** 095011
[5] Lan H., Osborne T.H., Groebner R.J., Snyder P.B., Xu G.S., Grierson B.A., Victor B.S., Leonard A.W. and Wang H.Q. 2020 H-mode pedestal improvements with neon injection in DIII-D *Nucl. Fusion* **60** 056013
[6] Ida K. *et al* 2009 Observation of an impurity hole in a plasma with an ion internal transport barrier in the large helical device *Phys. Plasmas* **16** 056111
[7] Dux R., Janzer A. and Pütterich T. 2011 Main chamber sources and edge transport of tungsten in H-mode plasmas at ASDEX Upgrade *Nucl. Fusion* **51** 053002
[8] Pütterich T., Dux R., Janzer M.A. and McDermott R.M. 2011 ELM flushing and impurity transport in the H-mode edge barrier in ASDEX Upgrade *J. Nucl. Mater.* **415** S334–9 Proc. 19th Int. Conf. on Plasma-Surface Interactions in Controlled Fusion
[9] Chilenski M.A., Greenwald M., Marzouk Y., Rice J.E. and White A.E. 2019 On the importance of model selection when

inferring impurity transport coefficient profiles *Plasma Phys. Control. Fusion* **61** 125012
[10] Geiger B. *et al* 2019 Observation of anomalous impurity transport during low-density experiments in W7-X with laser blow-off injections of iron *Nucl. Fusion* **59** 046009
[11] Sciortino F. *et al* 2020 Inference of experimental radial impurity transport on Alcator C-Mod: Bayesian parameter estimation and model selection *Nucl. Fusion* **60** 126014
[12] Sertoli M., Angioni C., Dux R., Neu R., Pütterich T. and Igochine V. 2011 Local effects of ECRH on argon transport in L-mode discharges at ASDEX Upgrade *Plasma Phys. Control. Fusion* **53** 035024
[13] Bruhn C. *et al* 2018 A novel method of studying the core boron transport at ASDEX Upgrade *Plasma Phys. Control. Fusion* **60** 085011
[14] Dux R. 2006 *STRAHL User Manual* (Max Planck Institute for Plasma Physics) (https://pure.mpg.de/rest/items/item_2143869/component/file_2143868/content)
[15] Odstrčil T., Howard N.T., Sciortino F., Chrystal C., Holland C., Hollmann E., McKee G., Thome K.E. and Wilks T.M. 2020 Dependence of the impurity transport on the dominant turbulent regime in ELM-y H-mode discharges on the DIII-D tokamak *Phys. Plasmas* **27** 082503
[16] Victor B.S. *et al* 2020 Impurity transport in the pedestal of H-mode plasmas with resonant magnetic perturbations *Plasma Phys. Control. Fusion* **62** 095021
[17] Sciortino F. *et al* 2021 Experimental inference of neutral and impurity transport in Alcator C-Mod using high-resolution x-ray and ultra-violet spectra *Nucl. Fusion* **61** 126060
[18] Fischer R., Fuchs C.J., Kurzan B., Suttrop W. and Wolfrum E. (ASDEX Upgrade Team) 2010 Integrated data analysis of profile diagnostics at ASDEX Upgrade *Fusion Sci. Technol.* **58** 675–84
[19] Chilenski M.A., Greenwald M., Marzouk Y., Howard N.T., White A.E., Rice J.E. and Walk J.R. 2015 Improved profile fitting and quantification of uncertainty in experimental measurements of impurity transport coefficients using Gaussian process regression *Nucl. Fusion* **55** 023012
[20] Kwak S., Svensson J., Bozhenkov S., Flanagan J., Kempenaars M., Boboc A. and Ghim Y.-C. 2020 Bayesian modelling of Thomson scattering and multichannel interferometer diagnostics using Gaussian processes *Nucl. Fusion* **60** 046009
[21] Ho A., Citrin J., Auriemma F., Bourdelle C., Casson F.J., Kim H.-T., Manas P., Szepesi G. and Weisen H. 2019 Application of Gaussian process regression to plasma turbulent transport model validation via integrated modelling *Nucl. Fusion* **59** 056007
[22] Chilenski M.A., Greenwald M.J., Hubbard A.E., Hughes J.W., Lee J.P., Marzouk Y.M., Rice J.E. and White A.E. 2017 Experimentally testing the dependence of momentum transport on second derivatives using Gaussian process regression *Nucl. Fusion* **57** 126013
[23] Foreman-Mackey D., Hogg D.W., Lang D. and Goodman J. 2013 emcee: the MCMC hammer *Publ. Astron. Soc. Pac.* **125** 306
[24] Neal R.M. 2011 MCMC using Hamiltonian dynamics *Handbook of Markov Chain Monte Carlo* vol 2 (Boca Raton, FL: CRC press) p 2
[25] Hoffman M.D. and Gelman A. 2014 The no-u-turn sampler: adaptively setting path lengths in Hamiltonian Monte Carlo *J. Mach. Learn. Res.* **15** 1593–623
[26] Bowman C., Harrison J.R., Lipschultz B., Orchard S., Gibson K.J., Carr M., Verhaegh K. and Myatra O. 2020 Development and simulation of multi-diagnostic Bayesian analysis for 2d inference of divertor plasma characteristics *Plasma Phys. Control. Fusion* **62** 045014
[27] Nishizawa T., Cavedon M., Dux R., Reimold F. and von Toussaint U. 2021 Plasma parameter profile inference from limited data utilizing second-order derivative priors and physic-based constraints *Phys. Plasmas* **28** 032504
[28] Barbui T., Carraro L., Den Hartog D.J., Kumar S.T.A. and Nornberg M. 2014 Impurity transport studies in the Madison symmetric torus reversed-field pinch during standard and pulsed poloidal current drive regimes *Plasma Phys. Control. Fusion* **56** 075012
[29] Cui Z.Y. *et al* 2013 Enhancement of edge impurity transport with ECRH in the HL-2A tokamak *Nucl. Fusion* **53** 093001
[30] Dux R., Cavedon M., Kallenbach A., McDermott R.M. and Vogel G. (the ASDEX Upgrade team) 2020 Influence of CX-reactions on the radiation in the pedestal region at ASDEX Upgrade *Nucl. Fusion* **60** 126039
[31] Fonck R.J., Darrow D.S. and Jaehnig K.P. 1984 Determination of plasma–ion velocity distribution via charge-exchange recombination spectroscopy *Phys. Rev.* A **29** 3288–309
[32] McDermott R.M. *et al* 2018 Evaluation of impurity densities from charge exchange recombination spectroscopy measurements at ASDEX Upgrade *Plasma Phys. Control. Fusion* **60** 095007
[33] McDermott R.M. *et al* 2017 Extensions to the charge exchange recombination spectroscopy diagnostic suite at ASDEX Upgrade *Rev. Sci. Instrum.* **88** 073508
[34] Viezzer E., Pütterich T., Dux R. and Kallenbach A. 2011 Investigation of passive edge emission in charge exchange spectra at the ASDEX Upgrade tokamak *Plasma Phys. Control. Fusion* **53** 035002
[35] Janev R.K. and Smith J.J. 1993 Cross sections for collision processes of hydrogen atoms with electrons, protons and multiply charged ions *Atomic and Plasma–Material Interaction Data for Fusion. V. 4* (Vienna: International Atomic Energy Agency)
[36] Jeffreys H. 1998 *The Theory of Probability* (Oxford: Oxford University Press)
[37] Nornberg M.D., Den Hartog D.J. and Reusch L.M. 2018 Incorporating beam attenuation calculations into an integrated data analysis model for ion effective charge *Fusion Sci. Technol.* **74** 144–53
[38] von Toussaint U. 2011 Bayesian inference in physics *Rev. Mod. Phys.* **83** 943–99
[39] Beskos A., Pillai N., Roberts G., Sanz-Serna J.-M. and Stuart A. 2013 Optimal tuning of the hybrid Monte Carlo algorithm *Bernoulli* **19** 1501–34
[40] Creutz M. 1988 Global Monte Carlo algorithms for many-fermion systems *Phys. Rev.* D **38** 1228–38
[41] McDermott R.M., Dux R., Guzman F., Pütterich T., Fischer R. and Kappatou A. 2020 Development of $Ar^{+16}$ charge exchange recombination spectroscopy measurements at ASDEX Upgrade *Nucl. Fusion* **61** 016019
[42] Li D., Svensson J., Thomsen H., Medina F., Werner A. and Wolf R. 2013 Bayesian soft x-ray tomography using non-stationary Gaussian processes *Rev. Sci. Instrum.* **84** 083506